Shock Compression of Monocrystalline Copper: Atomistic Simulations

BUYANG CAO, EDUARDO M. BRINGA, and MARC ANDRÉ MEYERS

Molecular dynamics (MD) simulations were used to model the effects of shock compression on [001] and [221] monocrystals. We obtained the Hugoniot for both directions, and analyzed the formation of a two-wave structure for the [221] monocrystal. We also analyzed the dislocation structure induced by the shock compression along these two crystal orientations. The topology of this structure compares extremely well with that observed in recent transmission electron microscopy (TEM) studies of shock-induced plasticity in samples recovered from flyer plate and laser shock experiments. However, the density of stacking faults in our simulations is 10^2 to 10^4 times larger than in the experimental observations of recovered samples. The difference between experimentally observed TEM and calculated MD results is attributed to two effects: (1) the annihilation of dislocations during post-shock relaxation (including unloading) and recovery processes and (2) a much shorter stress rise time at the front in MD (< 1 ps) in comparison with flyer-plate shock compression (~1 ns).

DOI: 10.1007/s11661-007-9248-9

I. INTRODUCTION

MOLECULAR dynamics (MD) is currently capable of simulating the large-scale shock compression of crystals; simulations with several hundred million atoms can be carried out in current supercomputers (*e.g.*, Reference 1). The first MD simulations related to shock were conducted by Mogilevsky[2,3] who used static compression and observed the changes in structure in the compressed material. This early work revealed the generation of dislocations with an associated decrease in the deviatoric stresses during compression. These dislocation loops nucleated preferentially at point defects. Since then, a large body of work has been carried out, revealing the detailed nature of the defects generated. Most of these studies, pioneered by Holian and others, considered the cases in which shocks travel along the [100], [110], and [111] directions.[4–7]

Holian and Lomdahl[3–5] found, for [100] fcc monocrystals, that plasticity occurred by stacking-fault nucleation. The nucleation threshold was extremely high for homogeneous nucleation, but low in the presence of preexisting defects. There are several other studies of shocks in single crystals along the main symmetry directions,[8,9] and one along a nonsymmetric direction on NiAl.[10]

Figure 1 shows, for conceptual clarity, how a shock front propagating along [001] interacts with the four slip systems; dislocation loops are generated in the slip planes. This is the schematic representation of the homogeneous nucleation mechanism.[11,12] Two situations are shown: (1) perfect and (2) partial dislocation generation. As they expand, the edge components move toward and away from the front and the screw components parallel to the front. These loops will, upon expansion, interact and generate dislocation reactions. Thus, the mobility of dislocations is severely hampered by the interactions. Since it is possible to generate either partial or perfect dislocation loops, this has a profound effect on the shock-induced structure. Whereas the screw components of perfect dislocations can cross-slip, partial dislocations cannot cross-slip and the resultant structure is marked by a large density of stacking faults and characterized by planar features. Meyers *et al.*[12] and Schneider *et al.*[13,14] characterized laser-generated shock structures in copper and copper-aluminum alloys, respectively. Tanguy *et al.*[15] developed a detailed analysis of the dislocation loop nucleation and growth in a shock wave. Nucleation was found to be thermally driven, whereas growth was the result of the relaxation of shear stresses. They obtained a critical diameter of the loop at which it expands as ~10 r, where r is the atomic radius. Germann *et al.*[16,17] demonstrated that the configuration of dislocations predicted by MD depends significantly on the crystal orientation (at pressures just above the Hugoniot elastic limit); they compared shock propagation along [100] and [111]. For [100], loops of partial dislocations were observed (such as in Figure 1(b)), whereas for [111] both leading and

BUYANG CAO, Postdoctoral Fellow, and MARC ANDRÉ MEYERS, Professor, are with the Materials Science and Engineering Program, Department of Mechanical and Aerospace Engineering, University of California, San Diego, La Jolla, CA, USA. Contact e-mail: bcao3@jhu.edu EDUARDO M. BRINGA, Physicist, is with the Materials Science Division, Lawrence Livermore National Laboratory, Livermore, CA, USA.

This article is based on a presentation made in the symposium entitled "Dynamic Behavior of Materials," which occurred during the TMS Annual Meeting and Exhibition, February 25–March 1, 2007 in Orlando, Florida, under the auspices of The Minerals, Metals and Materials Society, TMS Structural Materials Division, and TMS/ASM Mechanical Behavior of Materials Committee.

Article published online July 11, 2007

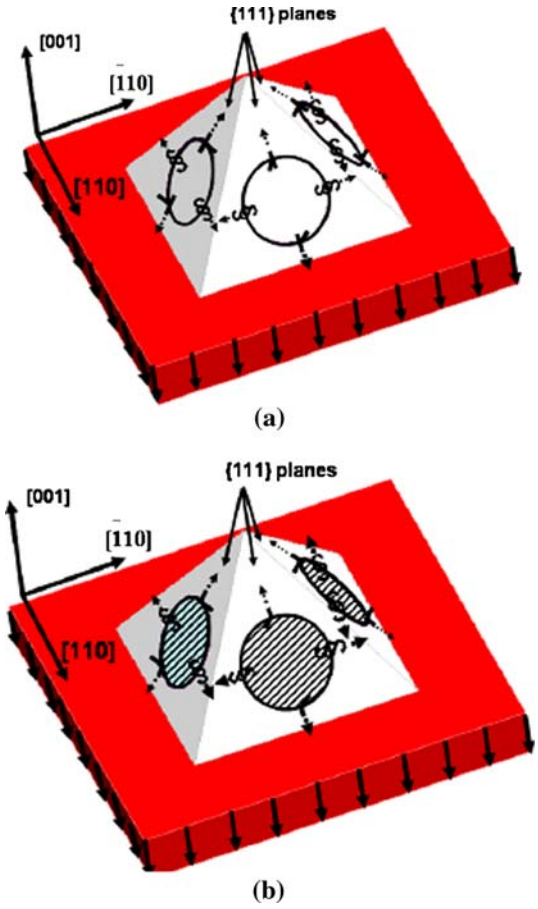

Fig. 1—Nucleation of dislocation loops at slip planes behind the shock front, which is in red (propagation along [001]): (*a*) perfect dislocations and (*b*) partial dislocations.

trailing partials were formed, leading to perfect dislocation loops which can cross-slip (such as in Figure 1(a)).

In the work presented here, we study a nonsymmetric orientation [221], enabling direct comparison of the defect structures with different experimentally tested crystal orientations. This is important for validating crystalline models of defect generation at the continuum scale, where the yield surface is strongly orientation dependent. Hence, the current work includes the comparison of both experimental and computational results on the shock compression of [001] and [221] monocrystalline copper over a wide pressure range.

II. COMPUTATIONAL METHODS

In our MD simulations, two perfect fcc Cu crystals, [001] and [221], were shock compressed at several pressures. The [001] monocrystalline copper has a dimension of $\sim 9 \times 9 \times 36$ nm^3 ($25 \times 25 \times 100$ fcc unit cells). This is sufficiently large to both calculate the shock Hugoniot and study the early stages of shock-induced plasticity, given that much larger simulations produce similar results.[7] For [100] shock propagation, the three coordinate axes were [100], [010], and [001]. The [221] monocrystal has a dimension of $\sim 15.3 \times 15.3 \times 65$ nm^3 ($42.42 \times 42.42 \times 180$ fcc unit cells) along the three coordinate axes of $[\bar{1}\bar{1}4]$, $[1\bar{1}0]$, and [221]. These dimensions are required for periodic boundary conditions in the lateral directions. The shock waves were produced as described previously, by a piston applied to the material at a velocity U_p.[1,9] The velocity of the shock wave, U_s, can then be calculated from the propagating front in our samples. The shock pressure can be calculated both from our MD simulations and from the Hugoniot relationship, once U_s and U_p are known.

We used the embedded-atom method (EAM) potential for Cu of Mishin *et al.*,[18] which was fitted to give a stacking-fault energy of 45 mJ/m^2, in agreement with some experiments. This potential gives a Hugoniot along the main symmetry directions, which agrees with the limited available experimental data.[9] Simulations were carried out using the large atomic/molecular massive parallel simulator.[19]

III. SHOCK PROPAGATION AND DEFECT PRODUCTION

The progression of the shock front through the specimens is shown in Figure 2; Figure 2(a) corresponds to [001] and Figure 2(b) to [221]. The defect structure is relatively unchanged during the advance of the front. For both orientations, we observe the nucleation and growth of stacking-fault loops, as observed previously for Lennard–Jones and EAM crystals.[4–7,9,15–17]

Sequential snapshots of the flow velocity of the atoms in the sample enable the calculation of the shock-wave velocity for the two orientations. Figure 3 shows the shock wave at three times, for (1) the [001] and (2) the [221] orientations at $U_p = 1$ km/s. The wave front is in the right-hand side, and the rigid piston on the left side. Note that a plastic front exists for [001], but does not lead to a two-front structure, as noted previously.[16] On the other hand, for the shock along [221], the front splits into an elastic precursor and a plastic front, as shown in Figure 3(b). Splitting of the elastic and plastic shock has been observed for the [111] and [110] directions.[9,16] The elastic wave itself is not stable for nonsymmetric directions in a cubic crystal, based on the kinematic analysis by Born and Huang.[20] Note that the elastic wave front is located near the bottom of Figure 2(b)(3), but elastic compression alone does not show as "defective" atoms.

Figures 4(a) and (b) show the pressure and the shear stress for the shock propagation along [001] (top) and [221] (bottom), for the three times shown in Figure 3. The shear stress, σ_{sh}, was calculated as $\sigma_{sh} = 0.5[\sigma_{zz} - 0.5(\sigma_{xx} + \sigma_{yy})]$, since the off-diagonal terms in the stress tensor were found to be negligible. For [221], the decrease in shear stress (Figure 4(d)) coincides with the pressure rise that leads to dislocation nucleation and the formation of a plastic front. As expected,[1,16] the shear stress relaxes because of dislocation loop nucleation and growth at the plastic front. For [001]

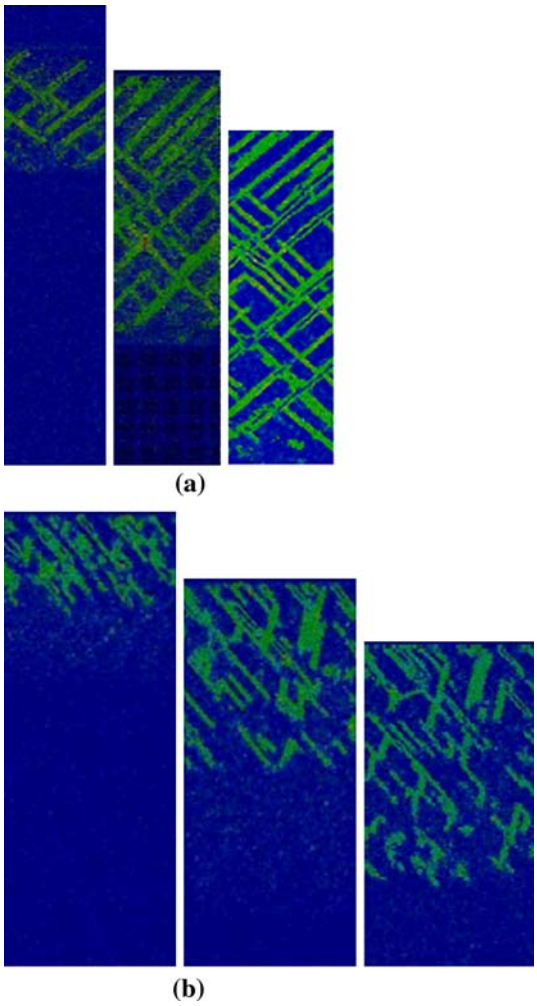

Fig. 2—Propagation of shock at piston/particle velocity U_p = 1 Km/s (48.5 GPa) for (*a*) [001] and (*b*) [221] at increasing times: (1) 2 ps, (2) 4 ps, and (3) 6 ps. Light colors indicate stacking faults and dislocations.

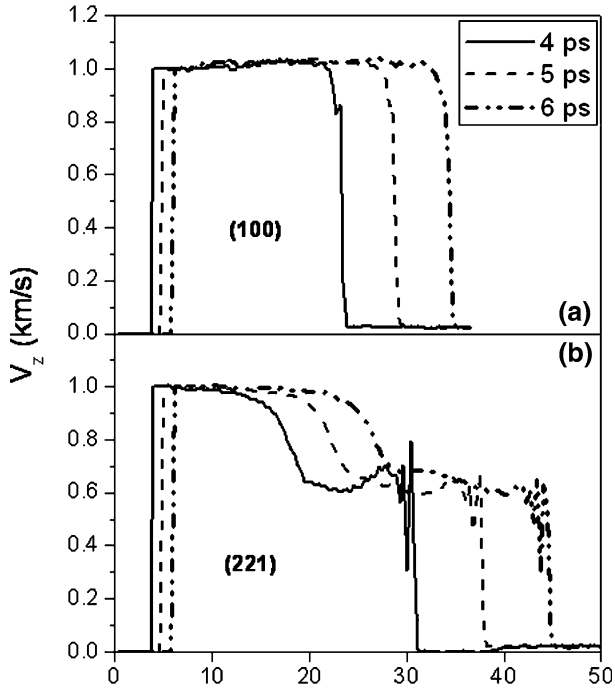

Fig. 3—Piston/particle velocity *vs* distance for shock propagation along (*a*) [001] and (*b*) [221].

(Figure 4(a)), this relaxation occurs within a region extremely close to the shock front.

The change of shock velocity, U_s, obtained from the simulation, with the particle/piston velocity, U_p, along [221] is plotted in Figure 5 and includes both the elastic and plastic wave velocities. Our [100] results are not shown, since they follow the calculations by Bringa *et al.*[9] for the same potential. Note that both the elastic and the plastic wave approach each other and the experimental Hugoniot for a polycrystal (U_s~ 4.0 + 1.5 U_p) only at pressures near melting, as was seen for [111] and [011] directions.[9]

The defect structures generated in our simulations are shown in greater detail in the three-dimensional views of Figure 6(a) for [001] and Figure 6(b) for [221]. For [001], shock propagation creates four stacking-fault traces (two in a plane view); the four variants have approximately the same frequency. These traces make angles of 45 deg with the lateral surface plane (010), as one expects from crystallography analysis. The [001] crystal orientation has eight slip systems with the same resolved stress. This is also implied by the schematic in Figure 1. The spacing of dislocation sources (loops) determines the mean length of the stacking-fault segments observed in Figure 6(a); the average loop diameter is equal to ~9 nm. The spacing (perpendicular to the loop plane) is approximately one third of this: ~3 nm. There is a degree of self-organization among the stacking faults, as one sees groups of parallel ones. As discussed by Schneider *et al.*[14] there seems to be some competition among them, the faster ones stopping the slower ones or the ones that nucleated later. This aspect of self-organization deserves further study. The two traces of stacking-faults in the [221] crystal make an angle of approximately 55 deg. This corresponds to the traces of two slip systems: one with highest resolved shear stress $(11\bar{1})[101]$, or $(11\bar{1})[011]$, and another one from $(\bar{1}11)[101]$, or $(1\bar{1}1)[011]$.

The transmission electron microscopy (TEM) micrographs mounted in a three-dimensional manner for the [001] and [221] crystals are shown in Figures 6(c) and (d). These results will be discussed in greater detail in the companion article.[21] The defect structures were observed by TEM in [001] and [221] monocrystalline copper specimens subjected to plate impact (pressure ~30 GPa; pulse duration ~1 μs). Stacking-fault packets were generated in [001] monocrystalline copper, and microbands were formed in [001]. The simulated defect structures in Figures 6(a) and (b) are similar to the TEM observations in Figures 6(c) and (d), for $(\bar{1}00)$ and (001) surfaces in a [001] monocrystal and $(1\bar{1}0)$ and (221) surfaces in a [221] monocrystal, respectively. However, it should be emphasized that the simulations are at a much smaller spatial scale.

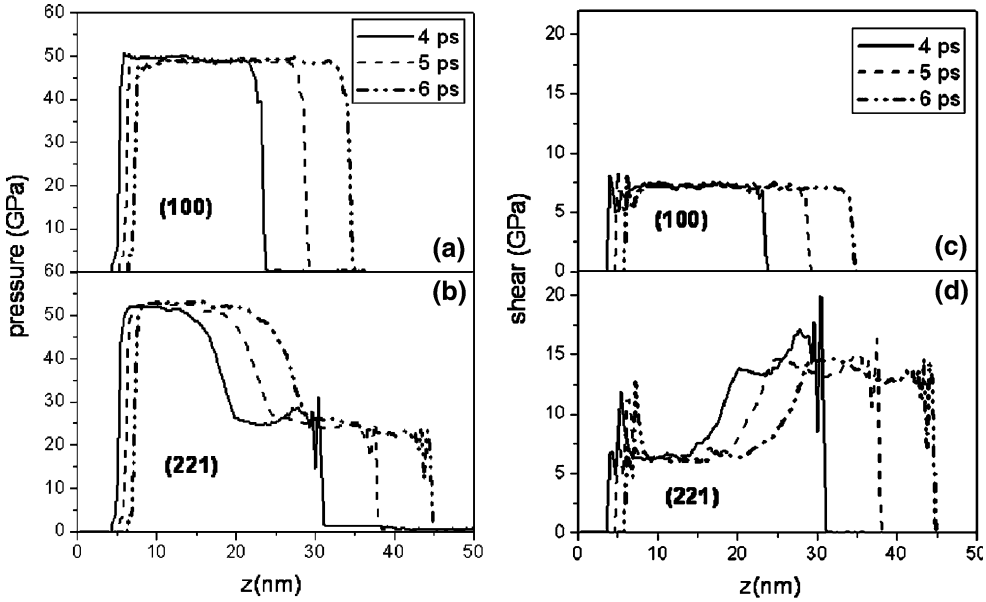

Fig. 4—Pressure profiles at three different times for (*a*) [001] and (*b*) [221] monocrystals; and shear stress profiles at different times for (*c*) [001] and (*d*) [221] monocrystals.

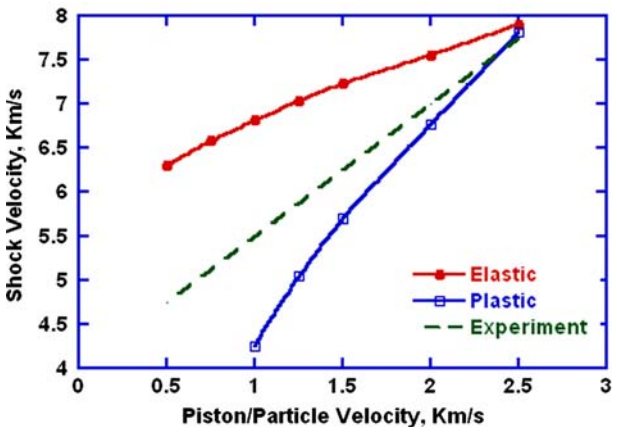

Fig. 5—Shock *vs* piston/particle velocities for elastic and plastic shock fronts in [221] shock propagation (compared with experimental results for polycrystals).

The traces of the slip systems on the $(1\bar{1}0)$ surface for the [221] monocrystal are schematically shown in Figure 7(a), with the enlarged picture from MD simulation showing the atoms in their regular fcc lattice positions in dark blue, while the atoms off their regular fcc symmetry and "tagged" by the center-of-symmetry algorithm (in LAAMPS or centro symmetric parameter (CSP)) are in green.

The simulations show that, as the piston (equivalent-to-particle) velocity is increased, the defect density increases. The sequence of snapshots in Figure 8 represents a range of pressures from 33.9 to 171.3 GPa for the [221] crystal. Note that the density of defects for P = 171.3 GPa (U_p = 2.5 km/s) is extremely high and the material resembles a nearly amorphous material. The shock-melting pressure for this EAM copper was calculated as ~200 GPa.[9] The corresponding defect spacing as a function of pressure is shown in Figure 9.

IV. COMPARISON OF COMPUTATIONAL AND EXPERIMENTAL RESULTS

The computational results obtained here can be converted into more fundamental deformation parameters through the determination of "shock-induced plasticity," a parameter introduced by Holian and Lomdahl.[5] Shock-induced plasticity was defined as a_0/l, where a_0 is the lattice constant (0.3615 nm for copper), and l is the average spacing between stacking faults. The results from our simulations are shown in Figure 10 for both [100] and [221] shocks, compared with their simulations (using different sample cross-sections) and simulations by Shehadeh *et al.*[21] The results are similar despite the fact that we used an EAM potential, whereas a Lennard–Jones potential was used in Reference 5. Shehadeh *et al.*[21] used the same EAM potential used here. A second parameter defined by Holian and Lomdahl[5] is the shock-induced strength, which is the ratio between the particle and sound velocities, U_p/c_0. The shock–induced plasticity increases monotonically with shock strength and follows closely the total volumetric strain U_p/U_s. Given that the total lateral strain in our simulations is zero due to periodic boundary conditions, the elastic strain has the same magnitude than the plastic strain, given by Orowan's equation.[1] The amount of dislocation motion needed to relax a given volumetric strain would be roughly the same for similar materials. Therefore, it would be expected that shock-induced plasticity would follow the total volumetric strain, even for different shock propagation directions and slightly different materials.

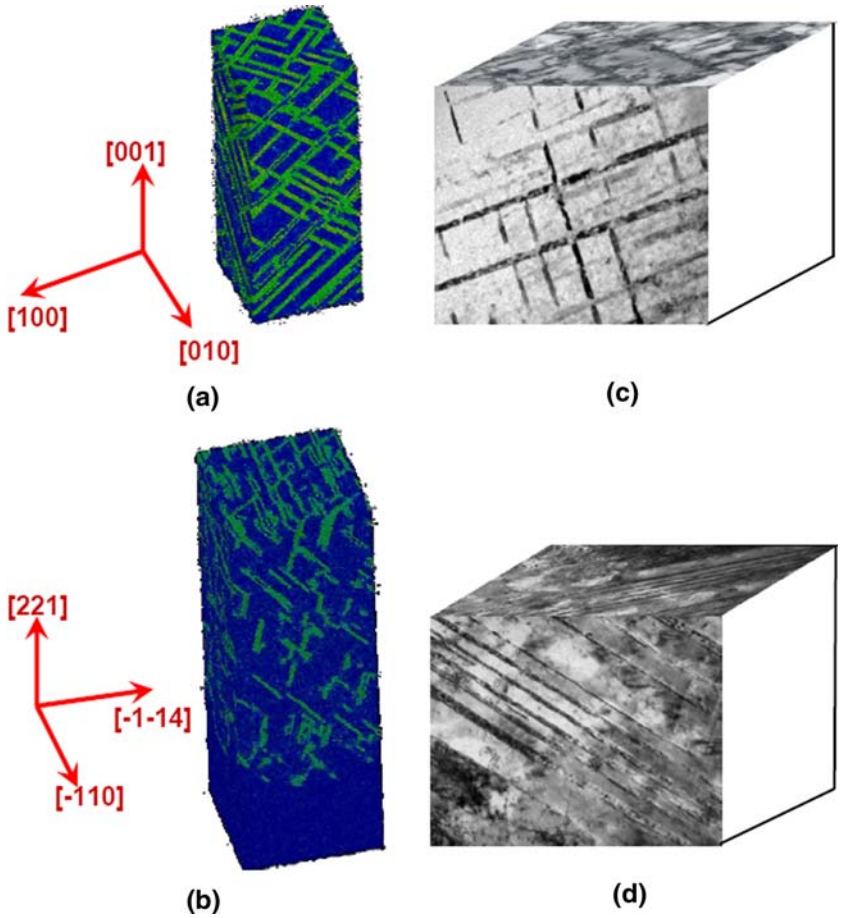

Fig. 6—Defect structures: (*a*) MD simulation results for 48.5-GPa shock propagation along [001], (*b*) MD simulation for 48.5-GPa shock propagation along [221], (*c*) TEM micrograph for [001] monocrystal shocked at 30 GPa, and (*d*) TEM micrograph on [221] monocrystal shocked at 30 GPa.

Experimental measurements in the literature extracted from TEM images for laser-shocked copper monocrystals subjected to a broad range of pressures[12–14,23] were converted into shock-induced plasticity; the corresponding pressures were converted to shock strengths. The results for laser shock are plotted in Figure 11(a); they correspond to the spacing between stacking-fault packets. The same monotonic increase in shock-induced plasticity with shock strength, as in Figure 10, is observed. However, there is a major difference: the values are lower by a factor of 10^4.

Plate impact[22,24–30] experiments on copper have been conducted since the 1970s. Classical among these experiments are the systematic measurements made by Murr and co-workers[24–28] on intertwin and interstacking-fault spacings. Figure 11(b) shows the shock-induced plasticity calculated using the intertwin spacings observed by Murr and co-workers,[24–28] and the work to be reported in the companion article.[22] Jarmakani *et al.*[30] found similar results. The shock-pulse duration in Murr's experiments[24–28] was ~2 μs, which is in the same range as our work in the companion article (1.4 to 2 μs).[22] Work by Andrade *et al.*[29] confirms the twin spacing experimentally observed by Murr.[24–28] The calculated shock-induced plasticity from Murr's data is on the order of 10^{-4}, which is smaller than the experimental results of the companion article (~10^{-3}).[22] These results, as well as the shock-induced plasticity in the laser-shocked samples of ~10^{-5} shown in Figure 11(a), are compelling evidence for major effects that are not generally considered, leading to spacing between defects observed in simulations that is much smaller than that observed by TEM on recovered samples. There are several possible reasons for this discrepancy: (1) the higher strain rate in MD simulations; (2) simulation of only a small volume of perfect single crystal, without any initial defects;[1] and (3) the possibility that most defects are annealed out[1] and that TEM observations reveal a structure that is completely different from the one extant during shock compression. In our simulations, if we allow for the shock wave to reach the back of the sample and produce a rarefaction wave, most of the stacking-fault network disappears, making clear the important role that recovery can play in the TEM samples. Dynamic X-ray diffraction may be able to probe the dynamic dislocation generation seen in MD simulations in the near future (*e.g.*, References 1 and 31).

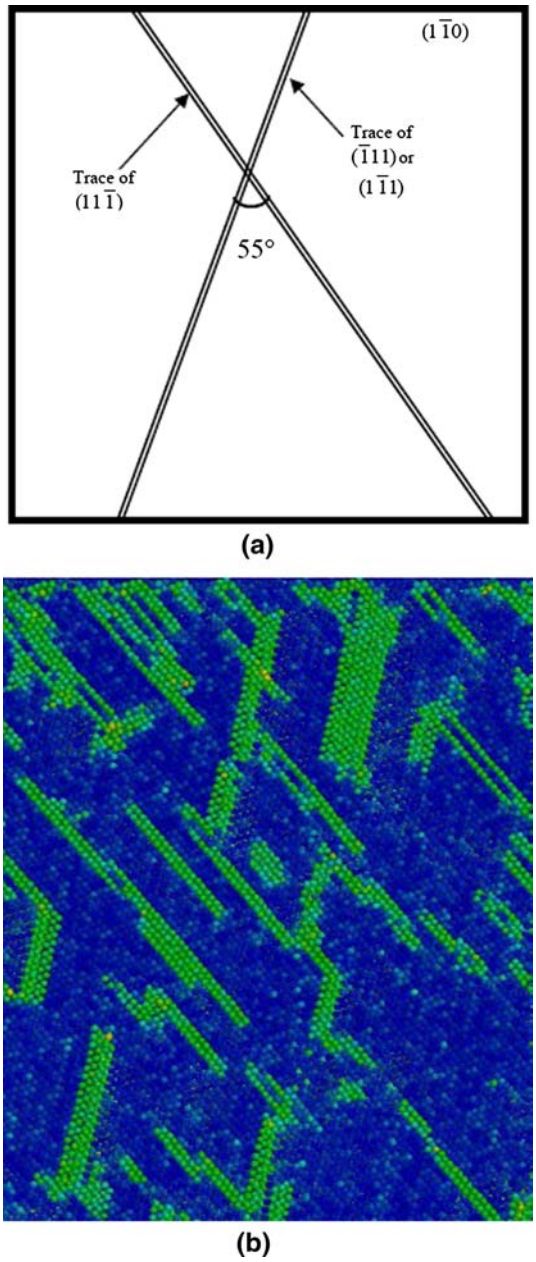

Fig. 7—(*a*) Schematic illustration of traces of {111} slip planes on the surface of a (1$\bar{1}$0)plane and (*b*) MD simulation showing traces of the stacking faults slip systems on the surface of (1$\bar{1}$0), shown by MD simulation for shock propagation along [221].

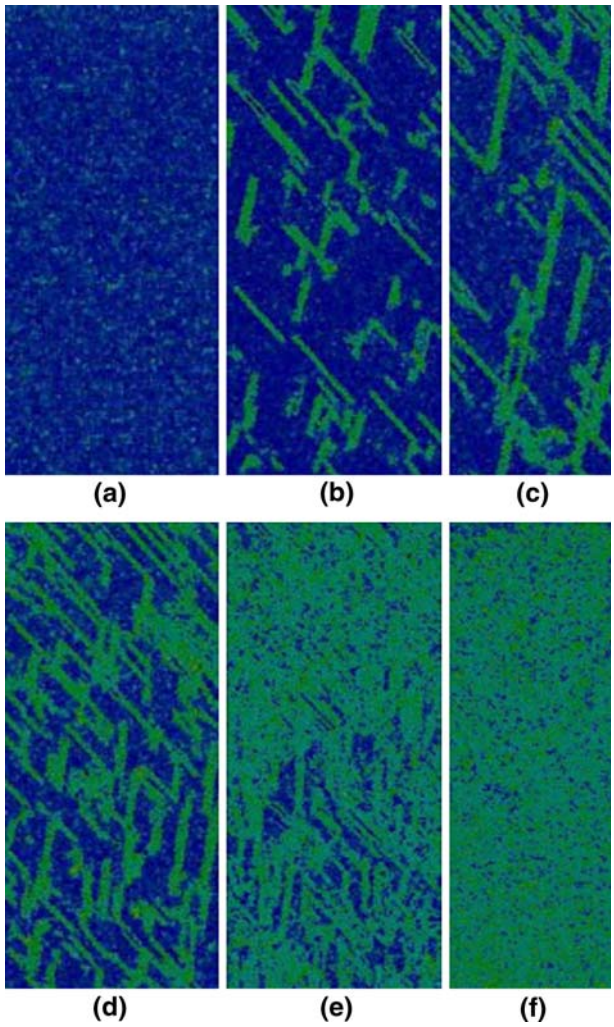

Fig. 8—Dislocation structures at 8 ps in shocked [221] as a function of particle/piston velocity: (*a*) 0.75 (33.9 GPa), (*b*) 1 (48.5 GPa), (*c*) 1.25 (64.8 GPa), (*d*) 1.50 (82.8 GPa), (*e*) 2.00 (123.7 GPa), and (*f*) 2.5 Km/s (171.3 GPa).

V. CONCLUSIONS

Simulations with MD were used to model the effects of shock compression on [001] and [221] monocrystals. We analyzed the shock profiles and obtained the shock Hugoniot for both orientations. As expected, we found the following.

1. The crystal orientation has a strong effect on the resulting defect microstructure.
2. The shock pressure has an effect on the density of defects.The simulated defect microstructure compares well with TEM observations of recovered

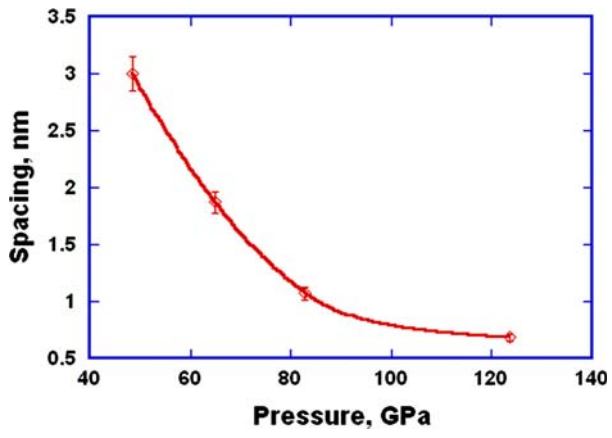

Fig. 9—Spacing between defects as a function of pressure for shock propagation along [221].

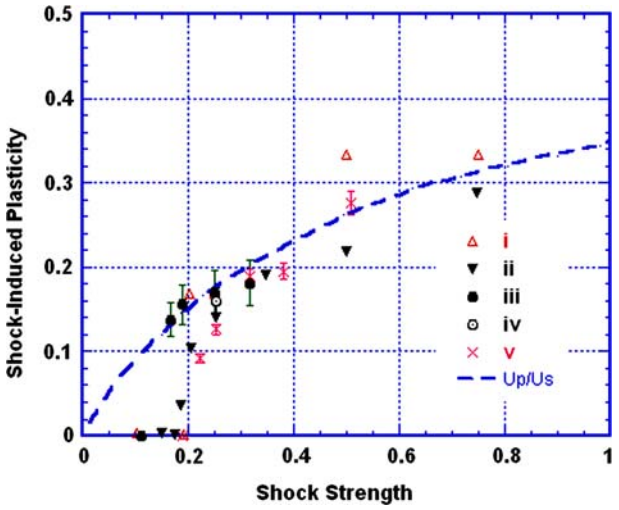

Fig. 10—Shock wave–induced plasticity a_0/lvs shock strength U_p/C_0 for different cross sections, in units of a_0^2: Holian and Lomdahl, Lennard–Jones solid, [001] direction,[5] 6×6 cross section (i) and 100×100 cross section (ii) Shehadeh *et al.*,[21] Cu Mishin EAM, 50×50 cross section, and [001] direction (iii). This work, Cu Mishin EAM, 25×25 cross section and [001] direction (iv), and 42×42 cross section and [221] direction (v).

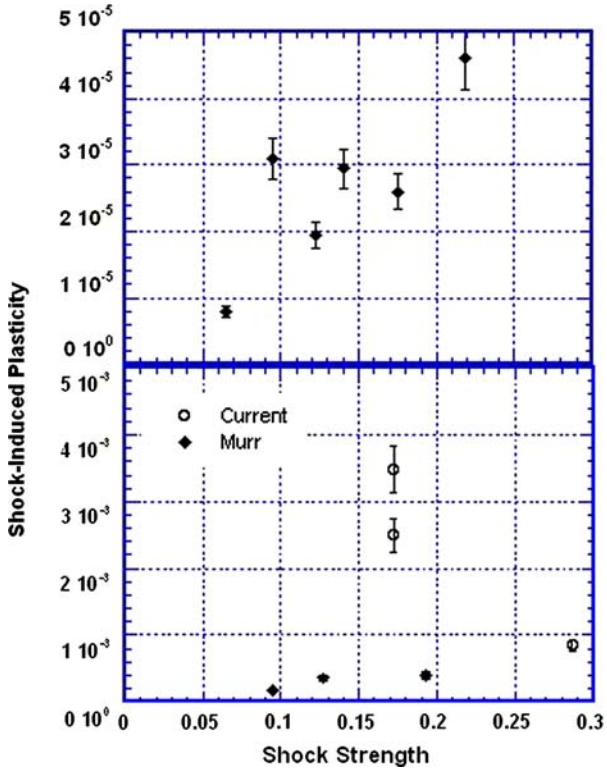

Fig. 11—Shock-induced plasticity calculated from experimental results: (*a*) laser shock[23] and (*b*) plate impact.[28]

samples. However, the simulated density of defects is orders of magnitude (10^2 to 10^4) higher than the experimental density. This could indicate that most of the defects generated during shock compression are annihilated before TEM observation. We also note that longer rise times during loading, such as the ones used in experiments, would lead to lower dislocation densities.[1] Another possible source of the difference is that the strain rate in the MD simulation, calculated from the stress rise time at the shock front ($\dot{\varepsilon} \sim 10^{9-12}\ s^{-1}$) is higher than typical experimental strain rates ($\dot{\varepsilon} \sim 10^{7-9}\ s^{-1}$), and that this difference in strain rate is responsible for the vast differences in defect spacing.

ACKNOWLEDGMENTS

This research was supported by the Department of Energy through Grant Nos. DEFG0398DP00212 and DEFG0300SF2202. The work at the Lawrence Livermore National Laboratory (LLNL) was performed under the auspices of the United States Department of Energy by the University of California, LLNL, under Contract No. W-7405-Eng-48. Mr. H. Jarmakani provided generous help in the preparation of figures. Discussions with Drs. P. Lomdahl and M.S. Schneider about the difference between MD and experimental stacking-fault spacing are gratefully acknowledged.

REFERENCES

1. E.M. Bringa, K. Rosolankova, R.E. Rudd, B.A. Remington, J.S. Wark, M. Duchaineau, D.H. Kalantar, J. Hawreliak, and J. Belak: *Nat. Mater.*, 2006, vol. 5, pp. 805–09.
2. M.A. Mogilevsky, V.V. Efremov, and I.O. Mynkin: *Combust., Explos., Shock Waves*, 1977, vol. 13, pp. 637–40.
3. M.A. Mogilevsky and I.O. Mynkin: *Combust., Explos., Shock Waves*, 1978, vol. 14 (5), pp. 680–83.
4. B.L. Holian: *Phys. Rev. A*, 1988, vol. 37A, pp. 2562–68.
5. B.L. Holian and P.S. Lomdahl: *Science*, 1998, vol. 280, pp. 2085–88.
6. K. Kadau, T.C. Germann, P.S. Lomdahl, and B.L. Holian: *Science*, 2002, vol. 296, pp. 1681–84.
7. B.L. Holian: *Shock Waves*, 2004, vol. 13, pp. 489–95.
8. V.V. Zhakhovskii, S.V. Zybin, K. Nishihara, and S.I. Anisimov: *Phys. Rev. Lett.*, 1999, vol. 83, pp. 1175–78.
9. E.M. Bringa, J.U. Cazamias, P. Erhart, J. Stolken, N. Tanushev, B.D. Wirth, R.E. Rudd, and M.J. Caturla: *J. Appl. Phys.*, 2004, vol. 96, pp. 3793–99.
10. A. Strachan and S.H. Luo: *Theoretical Division Nuclear Weapons Program Highlights*, Los Alamos National Laboratory, Los Alamos, NM, 2004–2005, pp. 78–79.
11. M.A. Meyers: *Scripta Metall. Mater.*, 1978, vol. 12, pp. 21–26.
12. M.A. Meyers, F. Gregori, B.K. Kad, M.S. Schneider, D.H. Kalantar, B.A. Remington, G. Ravichandran, T. Boehly, and J.S. Wark: *Acta Mater.*, 2003, vol. 51, pp. 1211–28.
13. M.S. Schneider, B. Kad, D.H. Kalantar, B.A. Remington, E. Kenik, V. Lubarda, and M.A. Meyers: *Int. J. Impact Eng.*, 2005, vol. 32, pp. 473–507.
14. M.S. Schneider, B.K. Kad, F. Gregori, D. Kalantar, B.A. Remington, and M.A. Meyers: *Metall. Mater. Trans. A*, 2004, vol. 35A, pp. 2633–46.
15. D. Tanguy, M. Mareschal, P.S. Lomdahl, T.C. Germann, B.L. Holian, and R. Ravelo: *Phys. Rev. B*, 2003, vol. 68, pp. 144111 (1)–(10).
16. T.C. Germann, B.L. Holian, and P.S. Lomdah: *Phys. Rev. Lett.*, 2000, vol. 84, pp. 5351–54.
17. T.C. Germann, D. Tanguy, B.H. Holian, P.S. Lomdahl, M. Mareschal, and R. Ravelo: *Metall. Mater. Trans. A*, 2004, vol. 35A, pp. 2609–15.
18. Y. Mishin, M.J. Mehl, D.A. Papaconstantopoulos, A.F. Voter, and J.D. Kress: *Phys. Rev. B*, 2001, vol. 63, pp. 224106 (1)–(16).
19. S.J. Plimpton: *J. Comput. Phys.*, 1995, vol. 117, pp. 1-19, http://lammps.sandia.gov/index.html

20. M. Born and K. Huang: *Dynamical Theory of Crystal Lattices*, Oxford University Press, New York, NY, 1954.
21. M.A. Shehadeh, E.M. Bringa, H.M. Zbib, J.M. McNaney, and B.A. Remington: *Appl. Phys. Lett*., 2006, vol. 89, pp. 171918 (1)–(3).
22. B. Cao, D.H. Lassila, C. Huang, Y. Xu, and M.A. Meyers: University of California, San Diego, CA, unpublished research, 2006.
23. M.S. Schneider: Doctoral Dissertation, University of California, San Diego, CA, 2004.
24. L.E. Murr and D. Kuhlmann-Wilsdorf: *Acta Metall*., 1978, vol. 26, pp. 847–57.
25. B. Kazmi and L.E. Murr: *Scripta Metall*., 1979, vol. 13, pp. 993–97.
26. C.H. Ma and L.E. Murr: *Proc. 5th Int. Conf. on High Energy Rate Fabrication*, Denver, CO, 1977, vol.1, p.1.6.1.
27. E. Moin and L.E. Murr: *Mater. Sci. Eng*., 1979, vol. 37, pp. 249–69.
28. L.E. Murr: in *Shock Waves and High-Strain-Rate Phenomena in Metals*, Plenum Press, New York, NY, 1981, pp. 607-73.
29. U. Andrade, M.A. Meyers, K.S. Vecchio, and A.H. Chokshi: *Acta Metall. Mater*., 1994, vol. 42, pp. 3183–95.
30. H. Jarmakani, J.M. McNaney, and M.A. Meyers: *Mater. Sci. Eng*., 2006, in press.
31. D.H. Kalantar, J.F. Belak, G.W. Collins, J.D. Colvin, H.M. Davies, J.H. Eggert, T.C. Germann, J. Hawreliak, B.L. Holian, K. Kadau, P.S. Lomdahl, H.E. Lorenzana, M.A. Meyers, K. Rosolankova, M.S. Schneider, J. Sheppard, J.S. Stolken, and J.S. Wark: *Phys. Rev. Lett*., 2005, vol. 95, pp. 075502 (1)–(4).